Proton Properties in Mercury's Magnetotail: A Statistical Study

J.-T. Zhao[1] , **Q.-G. Zong[1]** , **J. A. Slavin[2]** , **W.-J. Sun[2]** , **X.-Z. Zhou[1]** , **C. Yue[1]** , **J. M. Raines[2]** , **and W.-H. Ip[3,4]**

[1]School of Earth and Space Sciences, Peking University, Beijing, China, [2]Department of Climate and Space Sciences and Engineering, University of Michigan, Ann Arbor, MI, USA, [3]Institute of Astronomy, National Central University, Jhongli, Taiwan, [4]Space Science Institute, Macau University of Science and Technology, Macau

Abstract This study investigates the properties of protons in the magnetotail plasma sheet of Mercury. By superposing 5-year measurements from the MESSENGER spacecraft, we obtain the average energy spectrum of protons in the plasma sheet, which can be fitted nicely by the Gaussian-Kappa model. The proton density, pressure, and energy spectral index κ are found to be higher on the dawnside than on the duskside. The proton temperature shows a clearly outward radial gradient. The field-aligned density profile indicates that the protons in the outer plasma sheet move adiabatically. The pitch angle distribution reveals the reflected fluxes to be always less than the incident fluxes and indicates the loss of protons due to their impact on the planetary surface.

Plain Language Summary Mercury has a miniature magnetosphere subject to intense solar wind forcing. This magnetosphere, among the smallest in the solar system, resembles the Earth's in many key respects. It is also an analog for other small and outside-driven magnetospheres, such as Ganymede's inside Jupiter's magnetosphere. Mercury does not have a significant atmosphere but a tenuous exosphere. Therefore, Mercury's magnetospheric ions are thought to come predominantly from the solar wind, and only about 10% of the ions are of planetary origin. This study presents a statistical picture of the protons in Mercury's magnetotail plasma sheet measured by the Fast Imaging Plasma Spectrometer (FIPS) onboard MESSENGER spacecraft. Many parameters are obtained through a best fit procedure with a Gaussian-Kappa distribution. The proton number density, proton pressure, and spectral index κ show clear dawn-dusk asymmetric features. The results also suggest that the motion of the protons is adiabatic in the outer plasma sheet and non-adiabatic in the central plasma sheet. Furthermore, the loss feature of the protons is also revealed by their asymmetric pitch angle distributions.

1. Introduction

Mercury is the innermost planet in the solar system, and it has a global intrinsic magnetic field closely aligned with the planet's spin axis (<0.8°). Its magnetic equator is shifted northward by ~0.2R_M from its geographic center; $R_M = 2{,}440$ km is Mercury's radius. The magnetic moment is around 195 nT·R_M^3, which is much smaller than that in Earth (Alexeev et al., 2010, Anderson et al., 2011, 2012). Interactions between Mercury's magnetic field and the solar wind form a miniature magnetosphere with the subsolar magnetopause at ~0.45R_M above the surface (Slavin et al., 2009; Winslow et al., 2013). Furthermore, Mercury only has a tenuous exosphere, which contains many heavy atoms and ions, such as sodium, oxygen, and helium (Potter & Morgan, 1985; Raines et al., 2013; Wurz et al., 2019; Zurbuchen et al., 2011). And protons are the most abundant ions (>90%) in Mercury's magnetosphere.

The magnetic flux loading-unloading process in Mercury's magnetosphere, that is, the magnetospheric substorm, has a time scale of only 2 to 3 min (Imber & Slavin, 2017; Slavin et al., 2010; Sun et al., 2015), which is caused by the low solar wind Alfvén Mach number (Slavin & Holzer, 1979; Scurry et al., 1994) and the small magnetosphere (Siscoe et al., 1975). The low solar wind Alfvén Mach number also produces many magnetic reconnection-generated structures in the magnetosphere, including flux transfer events near the magnetopause (Russell & Walker, 1985; Slavin et al., 2009), flux ropes (DiBraccio, Slavin, Imber, et al., 2015; Slavin et al., 2012; Sun et al., 2016; Smith et al., 2018; Zhao et al., 2019), and dipolarization fronts in the

magnetotail plasma sheet (Sundberg et al., 2012; Sun et al., 2016, 2018). These magnetic structures at Mercury resemble those at Earth, but they contain strong kinetic features.

Mercury's tail plasma sheet has been revealed to have dawn-dusk asymmetry. The plasma sheet is thicker on the dawnside than on the duskside (Poh et al., 2017a), and magnetic reconnection occurs more frequently on the dawnside plasma sheet (Sun et al., 2016). The heavy ions are found to be concentrated on the duskside plasma sheet, that is, the pre-midnight sector (Gershman et al., 2014; Raines et al., 2011), whereas there are more protons on the dawnside than on the duskside (Chen et al., 2019; Korth et al., 2014). In studies about the dawn-dusk asymmetry of Mercury's magnetotail, Korth et al. (2014) investigated the distribution of proton fluxes, and Chen et al. (2019) presented the proton momenta under the assumption of isotropic and Gaussian distributions (Gershman et al., 2013; Raines et al., 2011). Sun et al. (2017, 2018) have shown that the proton spectra are non-Maxwellian and can be fitted by Kappa distribution.

The proton motion in Mercury's magnetotail is adiabatic in the region outside the central plasma sheet as demonstrated in previous test-particle simulations (Delcourt et al., 2017) during magnetic quiet period. In other words, the first adiabatic invariant ($\mu = \frac{1}{2}mv_{\perp}^2/B$) conserves. The proton trajectories are chaotic and non-adiabatic in the central plasma sheet, because the curvature radii of magnetic field are comparable to the gyro-radii of protons of keV range. Both test-particle simulations (Delcourt et al., 2007; Ip, 1987) and observations (Sun et al., 2017, 2018) have shown that the energization of protons is non-adiabatic during the magnetospheric active interval. A further study based on in situ measurements is desirable to verify the adiabatic theory and the simulation results.

In Mercury's plasma sheet, the loss cone of protons ($\alpha < \arcsin\sqrt{\frac{B_{max}}{B_{eq}}}$) ranges from 0° to 20° (Poh et al., 2018). Protons within the loss cone would impact the planetary surface and being absorbed (hereinafter referred to as surface precipitation). Winslow et al. (2013) has shown that the averaged reflected fluxes are less than the incident fluxes, implying a partially loss of protons. Furthermore, Korth et al. (2014) shows a north-south asymmetry of proton fluxes in the magnetotail plasma sheet due to the northward shift of Mercury's magnetic dipole.

In this study, we analyze approximately 5 years of measurements from MESSENGER in Mercury's magnetotail (Andrews et al., 2007). We fit the proton spectra with the Gaussian-Kappa distribution to obtain the density, pressure and spectral index κ. Moreover, the proton pitch angle distributions (PADs) are used to investigate their loss mechanisms. The paper is organized as follows: Section 2 provides a description of the data set and the spatial superpose method. Section 3 shows statistical results of proton properties. The discussion and conclusion are presented in the last section.

2. Data and Methods

2.1. Magnetic Field and Ions Measurements

This study utilizes the data measured by the Magnetometer (MAG) and the Fast Imaging Plasma Spectrometer (FIPS) onboard MESSENGER. The MAG measured magnetic field vectors at a time resolution of 50 ms (Anderson et al., 2007). The FIPS measured energy spectra of ions (mass per charge from 1 to 60 amu/e) within the energy range from 46 to 13.6 keV/e in a limited field-of-view (FOV) of ~1.15π sr (Andrews et al., 2007). The time resolution of the FIPS data is 10 s, and the pitch angle resolution is 10°.

The magnetic field and spacecraft position are provided under Mercury Solar Magnetospheric (MSM) coordinate system. In MSM coordinates, X-axis points to the Sun, Z-axis points perpendicular to the orbital plane and is positive in the geographic northward direction, and Y-axis completes the right-hand system. The origin of the coordinate system is shifted northward by ~0.20R_M from the center of the planet because of the dipole field offset (Alexeev et al., 2010; Anderson et al., 2010). The spacecraft position is further rotated by an aberration angle around the Z-axis to enforce the aberrated X-axis to be anti-parallel to the solar wind (400 km/s). The new coordinate is referred to as aberrated MSM (aMSM) coordinate.

2.2. Spatial Superpose Analysis

Figure 1 introduces the method we used to investigate the proton parameters obtained from FIPS measurements. The magnetotail is divided into several grid boxes with a size of $\Delta\rho = 0.1R_M, \Delta\theta = 15°$ in polar coordinates (Figure 1f). When we investigate the distributions of proton properties in the equatorial plane
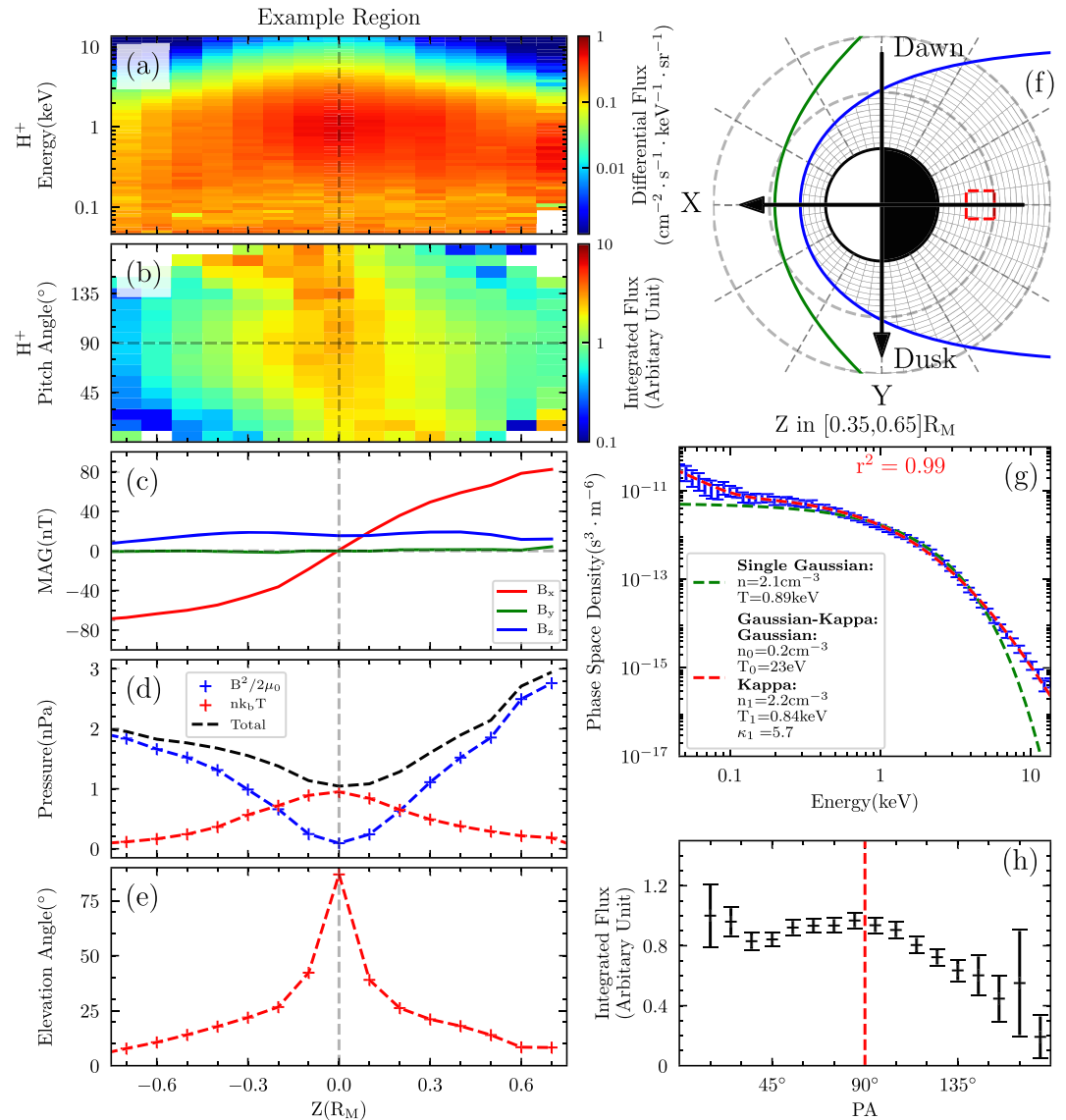
Figure 1. An example of superposed observation by FIPS (proton) and MAG. (a) Differential energy flux, (b) PAD normalized by average, (c) magnetic field, (d) pressure (magnetic and thermal), (e) elevation angle, (f) grid division schematic, (g) mean PSD at the selected regions, and (h) mean PAD normalized by maximum.

(section 3.1), the polar radius ρ is the distance to the Z-axis (i.e., $\sqrt{X^2 + Y^2}$) and the polar angle θ represents the local time ($\theta = (1 - \frac{\text{Local Time}}{24}) \times 360°$). When we investigate the distribution in the meridian plane (section 3.2), ρ represents the distance to the Y-axis (i.e., $\sqrt{X^2 + Z^2}$) and θ represents the magnetic latitude. Other panels in Figure 1 show the superposed measurements from FIPS and MAG by averaging each measurement inside the red box marked in Figure 1f ($-1.5R_M < X < -2.0R_M$ and $-0.25R_M < Y < 0.25R_M$) during the entire mission of MESSENGER (from 18 March 2011 to 30 April 2015).

In Figure 1a, the proton differential energy fluxes show a peak at the magnetic equator ($Z = 0$) in almost all energy channels, indicating that the number density and thermal pressure are the highest in the center of the plasma sheet. The PADs are clearly anisotropic and vary along the Z-axis (Figure 1b). Magnetic field observations (Figure 1c) demonstrate a reversed B_x and an enhanced B_z near the magnetic equator. The magnetic B_y component, on the other hand, is always very close to zero. In addition, the magnetic pressure (blue line in Figure 1d) is the lowest and the elevation angle ($\arctan(B_z/\sqrt{B_x^2 + B_y^2})$, Figure 1e) is the highest ($\sim 90°$) at the center of the plasma sheet comparing with those at the outer plasma sheet.

The mean phase space density (PSD) of protons from $Z = 0.35R_M$ to $Z = 0.65R_M$ is shown in Figure 1g as the blue line and the corresponding PAD is shown in Figure 1h. The error bars in these two panels represent the standard derivations of the mean for each data point. The proton energy spectrum is fitted in two ways as shown in Figure 1g. One is to fit the spectrum with a Gaussian distribution, which is shown as the dashed green line. The other approach, similar to the one used in Sun et al. (2017), is to fit the spectrum with a non-drifting Kappa distribution for high energy protons and a Gaussian for lower energy protons shown as the dashed red line. Here, the non-drifting Kappa distribution is written as

$$f(v) = \frac{n}{2\pi(\kappa\omega_\kappa^2)^{3/2}} \frac{\Gamma(\kappa+1)}{\Gamma(\kappa-1/2)\Gamma(3/2)} \left(1 + \frac{v^2}{\kappa\omega_\kappa^2}\right)^{-\kappa-1}, \tag{1}$$

where $\omega_\kappa = \sqrt{(2\kappa-3)k_B T/\kappa m_p}$ is the thermal velocity, m_p is the proton mass, n is the number density, T is the equivalent temperature, and Γ is the Gamma function. The Kappa distribution becomes a Gaussian when $\kappa \to \infty$. In Figure 1g, the single Gaussian distribution largely deviates from the measurements at low energy part ($<100\,\mathrm{eV}$) and high energy tail ($>5\,\mathrm{keV}$), whereas the Gaussian-Kappa (dashed red line) fits the measurements very well with a correlation coefficient (r^2) of ~0.99. In the Gaussian-Kappa fit, we obtain the number densities and thermal pressure by summing the Gaussian component (n_0, p_0) and the Kappa component (n_1, p_1). The ratio between the summed pressure and the density of the two components ($\frac{p_0+p_1}{k_B(n_0+n_1)}$) is defined as the proton temperature. The fitting parameters are listed in Table S1 in the supporting information.

Regarding the PAD (Figure 1h), asymmetric proton fluxes and loss cone distributions at the high latitude regions are clearly observed. The incident fluxes ($0° < PA < 90°$) are nearly isotropic and the reflected fluxes ($90° < PA < 180°$) gradually decreases as pitch angle increases. Such anisotropic PAD suggests that a fraction of protons is lost as they impact the surface of Mercury. This anisotropy is properly reflected in the estimated density since we used PSD that averaged through the entire pitch angle bins. The scalar temperature and pressure are not well-defined because they rely on the assumption of isotropic distribution. However, the estimation of plasma temperature would not be affected if we regard the temperature as a proxy of the mean kinetic energy.

Proton temperatures and densities in all spatial grids (Figure 1f) are obtained through a similar Gaussian-Kappa fitting procedure. In this study, both the cold Gaussian and the hot Kappa populations are considered when the proton density and thermal pressure are derived, although the cold population has in general very small contributions to the thermal pressure (~1%) and number density (~10%).

3. Proton Distributions in Mercury's Plasma Sheet

3.1. Proton Distributions near the Magnetic Equatorial Plane

The superposed proton spectrum obtained by averaging all the FIPS measurements inside each spatial grid is fitted with the Gaussian-Kappa distribution. The spatial grids span from $-0.2R_M$ to $0.2R_M$ in the Z direction of aMSM coordinate, which is close to the mean thickness of the plasma sheet (Poh et al., 2017a; Rong et al., 2018). The fit results, including proton number density (n_p), temperature (T_p), thermal pressure (P_p), and spectral index (κ), are shown in Figures 2a to 2d. Correlation coefficients (r^2) between the fit results and the measurements, together with the number of measurements, are shown in Figures 2e and 2f. As shown, the sample numbers are generally larger than 500, which ensure statistical significance. Besides, the correlation coefficients are close to 1 in almost all grid boxes, indicating that the fit results match well with the measurements. The n_p and P_p values are higher on the dawnside than on the duskside (Figures 2a and 2c). On the other hand, the T_p value is nearly dawn-dusk symmetric. The distribution of κ values in Mercury's magnetotail plasma sheet is provided for the first time (Figure 2d), and they are larger on the dawnside (~10) than on the duskside (<4), indicating that the protons in the dusk sector could have been accelerated.

Figures 2g and 2h display the particle fluxes of thermal protons (with the energy range from $830\,\mathrm{eV}$ to $13.6\,\mathrm{keV}$) and warm protons (from 46 to $830\,\mathrm{eV}$). The separation energy is selected to be the average temperature of protons in Mercury's plasma sheet (close to 1 keV). Therefore, the thermal protons (warm protons) refer to protons with kinetic energies higher (lower) than the mean kinetic energy. It is shown in Figure 2g,
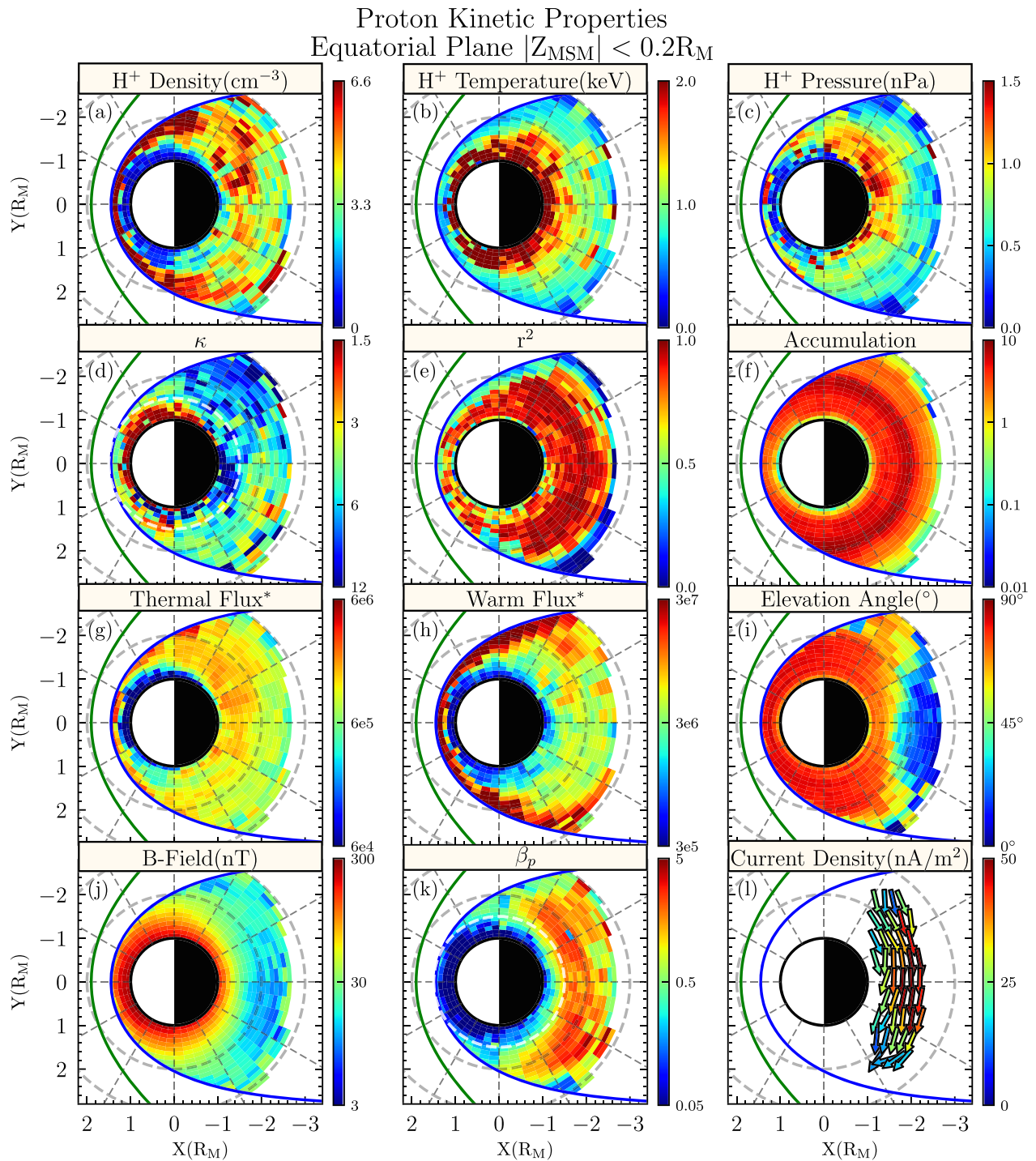
Figure 2. Proton kinetic properties in the magnetic equatorial plane with $|Z| < 0.2R_M$, (a–d) number density, temperature, thermal pressure, and Kappa estimated from Gaussian-Kappa model; (e) goodness of model fitting; (f) accumulations of FIPS's measurements; (g,h) differential energy flux in the combined two energy channels; (i) elevation angle; (j) mean magnetic field measured by MAG; (k) proton beta as a ratio of fitted thermal pressure and mean magnetic pressure; and (l) current density and direction obtained from finite difference of superposed $\vec{B}$.

the thermal protons concentrate in the near Mercury tail region and display a clear dawn-dusk asymmetry with higher fluxes on the dawnside. While the warm protons are mainly located further downtail symetrically near the magnetopause flanks.

The observed mean magnetic field is also shown in Figure 2j. In addition, the elevation angle ($\arctan(B_z/\sqrt{B_x^2 + B_y^2})$, Figure 2i) and proton beta ($n_p k T_p / \frac{B^2}{2\mu_0}$, Figure 2k) which represents the external magnetic field contributed from cross-tail currents and the relative importance of plasma pressure are also presented. Here, we show the median value of the elevation angle inside each grid box instead of the mean value because the latter would be strongly affected by the $\sim 90°$ elevation angles near the equatorial plane ($Z \approx 0$). The magnetic elevation angles (Figure 2i) are almost $90°$ in the equatorial plane near the planet and become smaller further downtail.

Figure 2l shows the distribution of electric current density in the equatorial plane, which is derived by computing the curl of the observed mean magnetic field ($\nabla \times \mathbf{B}/\mu_0$). The magnetic field is averaged over bin sizes of $0.2 R_M$ in each direction. The average magnetic field vectors are smoothed by their neighboring four vectors in the X-Y plane. As shown, the current directions (marked by the arrows) deviate from a straight dawn-dusk line, which indicates X-directional current components. The intensity of the current density (represented by the different colors) is higher on the midnight than on the flanks, which should be due to the fact that the plasma sheet is the thinnest near the midnight.

3.2. Proton Distributions in the Meridian Plane

Figure 3 shows the proton properties in the meridian plane. The distribution is binned in the ρ-z plane, where ρ is the distance to the Y-axis. These distributions accumulate the data points from magnetic local time 21:00 to 03:00. The open-closed field line boundary (see the white line in Figure 3e or the red lines in other panels) is obtained by tracing the average magnetic field at each position. The average magnetic field at each position is the mean field within a $0.2 R_M$ radius, and the iterated step is set to be $0.1 R_M$. The north initial point is set to be at the planetary surface with a latitude of 54°N, which is given by previous magnetic field model (KT14) (Korth et al., 2015). Meanwhile, the south initial point is set to be the mirror point of the north field line at $X = -1.35 R_M$ ($Z = -0.65 R_M$) because of the limited spatial coverage of observations. Several proton parameters, including density (Figure 3a), pressure (Figure 3c), and plasma β (Figure 3f), are enhanced inside the open-closed field line boundary. The proton parameters are reliable since the r^2 value is close to 1 in each grid (Figure 3e).

The temperature (~ 0.6 keV) and number density (~ 1.2 cm^{-3}) in the lobe region could also be obtained by averaging the observations. In addition, the characteristic Alfvén speed was estimated to be $V_A = B_L/\sqrt{\mu_0 n_p m_p} = 798$ km/s, where B_L is set to be 40 nT (Poh et al., 2017b). It should be noted that the proton energy spectrum in the lobe region contains only a small number of counts, which could lead to large uncertainty of the proton parameters in the lobe region.

According to the flux distributions shown in Figure 3g, the thermal protons are concentrated near the equatorial plane, whereas the warm protons (Figure 3h) are almost evenly distributed in the nightside plasma sheet, with the fluxes in the further tail region slightly higher than those in the nearer tail region.

When protons with some specified energy move adiabatically in the outer plasma sheet, they would bounce back and forth along magnetic field lines. If these adiabatic protons move along closed magnetic field lines, they would be trapped by the closed field lines to some extent (Korth et al., 2014). Hence, the regions where magnetic field lines are closed should be filled with trapped protons and have relative larger proton number densities. As a result, the boundary of open-closed field line would be a separation between high density and low density regions. The statistical result shown in Figure 3a reveals a field-aligned proton density profile. This signature implies the motion of protons is likely to be adiabatic otherwise the protons should distribute on each field line regardless of the field line topology. The distributions of proton temperature, pressure, and the integrated fluxes also demonstrate similar features that are correlated with the open-closed field line boundary.

4. Proton Loss in Mercury's Magnetotail

To study the proton loss in Mercury's magnetotail, the normalized loss ratio of protons ($[(J_{<90°} - J_{>90°})/(J_{<90°} + J_{>90°})]$) and the loss flux ($J_{<90°} - J_{>90°}$) are presented in Figure 4. Here, J is the
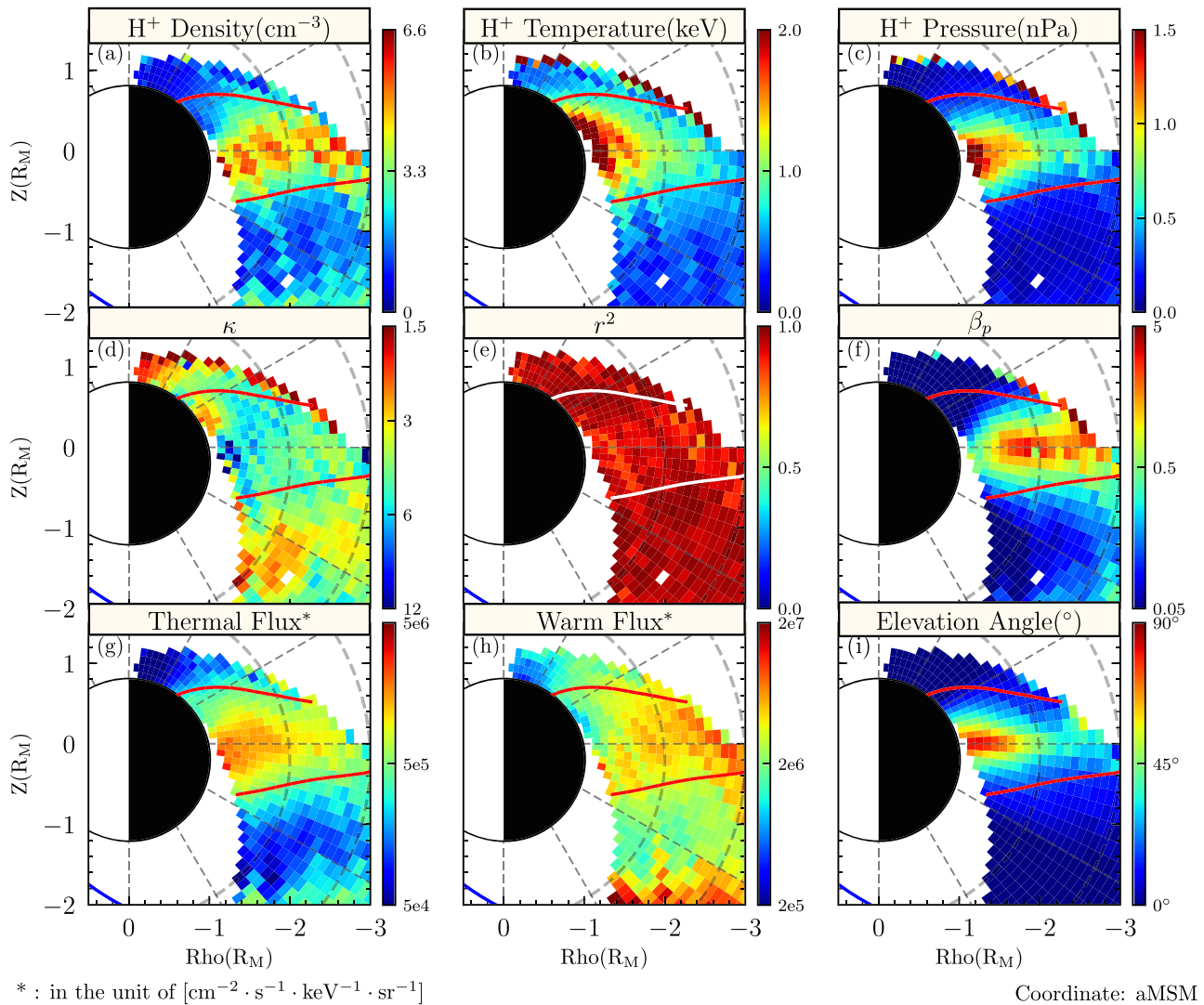
Figure 3. Same format as Figure 2 excluded the last three subplots in Figure 2.

integrated flux, and the subscript <90° (>90°) represents the pitch angle ranges. Both the loss ratio and the loss flux are positive (negative) when the reflected fluxes is less than the incident fluxes in the north (south) hemisphere (i.e., the incident fluxes are partially lost). Figures 4a and 4b demonstrate that the proton loss ratio and loss flux are anti-symmetric in the northern and southern hemispheres as expected. Figure 4d shows the distribution of the mean magnetic field measured by MESSENGER, together with several traced field lines inside the open-closed field line boundary. Pink dashed circles represent the gyro-radii (r_g) of protons with 1-keV perpendicular energy at each selected position, which could be compared with the curvature radii (r_c) of the mean magnetic field lines directly. This characteristic perpendicular energy of 1 keV is close to the proton temperature in Mercury's magnetotail plasma sheet, which means we can infer whether the motion of most protons is adiabatic or not by comparing the gyro-radii of these 1-keV protons with the magnetic field curvature radii. In the northern hemisphere, ∼5% of the protons are lost by their impact on the north surface of the planet. In the southern hemisphere, ∼15% of the protons are lost by their impact on the south surface of the planet. Such a north-south asymmetry might be produced by Mercury's offset-dipole center: The south surface is farther from the dipole center and the surface magnetic field intensity is weaker compared to the surface intensity at the same magnetic latitude in the northern
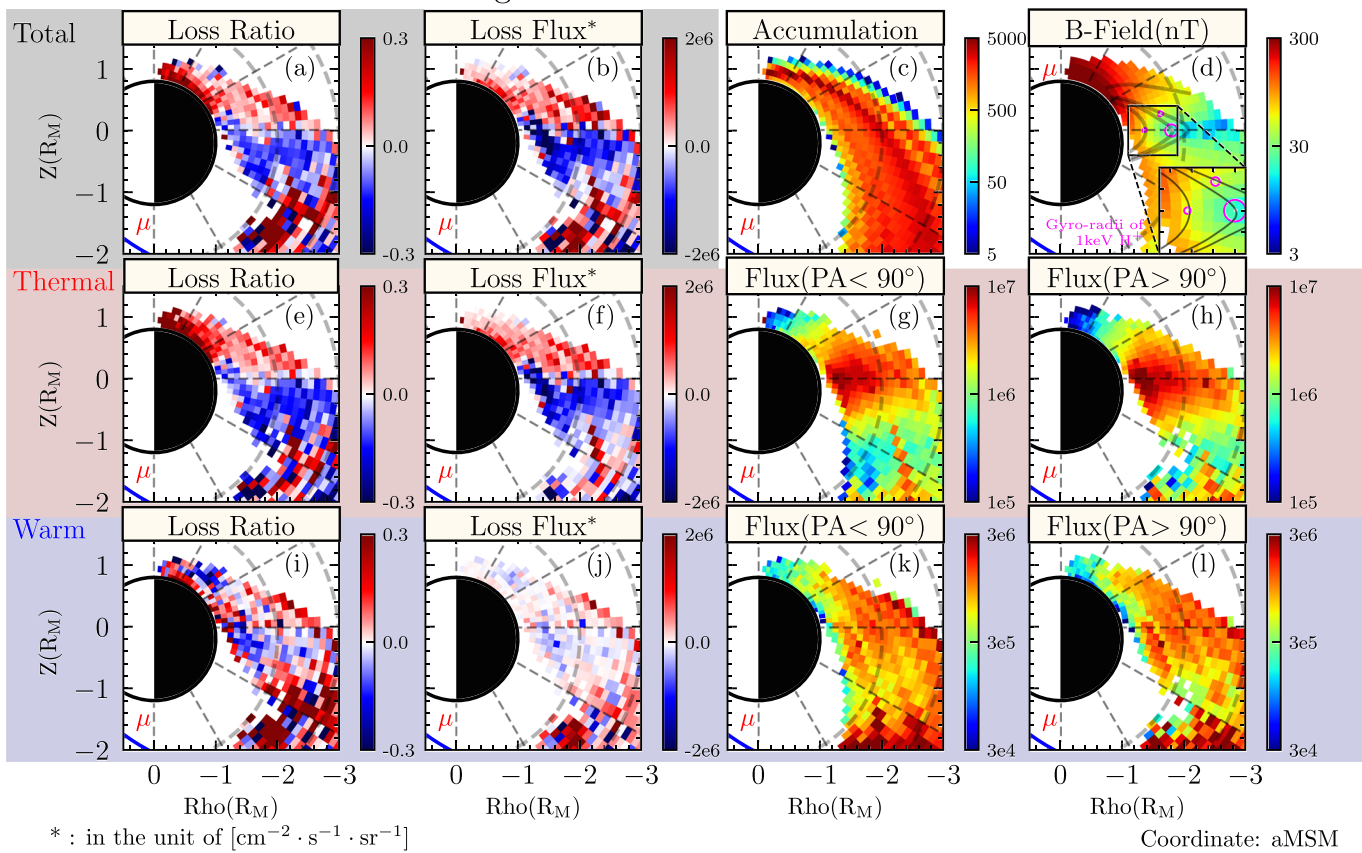
Figure 4. Loss ratio for different energy channels. (a,e,i) Normalized loss ratio for the all, thermal, and warm parts of proton; (b,f,j) the average loss flux for the three parts of proton; (c) accumulation of FIPS's measurements; (d) mean magnetic field intensity measured by MAG; and (g,h,k,l) integrated flux of thermal and warm components with pitch angle larger (less) than 90°.

hemisphere. For the magnetic latitude of 45°, the north and south surface dipole field intensities are 504 and 213 nT, respectively. Assuming the magnetic field intensity where the proton starts adiabatic motion is 40 nT, the loss cone is 4.6° and 10.8° for north and south hemisphere, respectively. Hence, more protons could hit the south surface and get lost.

Figures 4e to 4h show the loss ratio and loss flux as well as the fluxes with PA < 90° and PA > 90° of thermal proton, and the corresponding warm proton distributions are shown in Figures 4i to 4l. The loss feature of the thermal proton is very clear and similar to the features of protons that are integrated over the whole energy range (Figures 4a and 4b). However, the loss features of the warm protons are not so significant comparing to the loss features of the thermal protons. This result indicates that the thermal protons contribute most of the loss fluxes.

5. Discussion and Summary

Protons in Mercury's magnetosphere come from the solar wind and enter the magnetosphere via magnetopause and magnetotail magnetic reconnection (Zurbuchen et al., 2011). Since the magnetic reconnection occurs more frequently on the dawnside (Sun et al., 2016), there are more ejected protons which results in higher number density on the dawnside (Figure 2a). In addition, these protons on the dawnside would also be energized more significantly by the magnetic reconnection and reconnection-related processes, such as dipolarizations. These entry and energization processes produce the dawn-dusk asymmetry of thermal fluxes in the magnetotail plasma sheet, as shown in Figure 2g. The energization processes happen mostly on the closed magnetic field line regions, and therefore, the energized protons, that is, the thermal protons in Figure 3g, are predominately located inside the open-closed field line boundary.

The variation of proton density coincides the open-close field line boundary, which suggests that most protons in the outer plasma sheet are trapped. In the central plasma sheet, the magnetic field is weak and highly dynamic; hence, the proton motion is non-adiabatic and chaotic. The cross-tail current has an asymmetric X-directional component on the dawn and dusk sides, which results in a bent magnetotail current. This might be caused by the diamagnetic current ($\mathbf{J} = -\frac{\nabla p_{th} \times \mathbf{B}}{B^2}$, where p_{th} represents the thermal pressure of plasma).

Gyro-radii (r_g) of protons with 1-keV perpendicular energy at positions shown in Figure 4d are 75, 244, and 99 km (left, right center, and right upper), and the corresponding curvature radii (r_c) of the magnetic field lines are 603, 167, 23,000 km, respectively. These results suggest the existence of three types of motion in Mercury's magnetotail: adiabatic ($\sqrt{r_c/r_g} > 3$), chaotic ($3 > \sqrt{r_c/r_g} > 1$), and Speiser orbits ($1 > \sqrt{r_c/r_g}$) (Bchner & Zelenyi, 1989). Therefore, the motion of protons in the outer magnetotail plasma sheet could be described as gyro-bounce-drift motion similar to the protons in Earth's inner magnetosphere. Previous studies (DiBraccio, Slavin, Raines, et al., 2015; Jasinski et al., 2017) suggest a ~20-km/s equatorial convection speed due to the $\mathbf{E} \times \mathbf{B}$ drift. By assuming the proton in the inner magnetotail region ($\rho < 1.5 R_M$) is transported from the tailward regions, the protons would be energized as they are convected inward, which is consistent with our statistical result shown in Figure 2b. However, the radial variation of κ value indicates this energization process may not be adiabatic. The dawn-dusk asymmetry of κ value also demonstrate the strong non-adiabatic cross-tail acceleration in Mercury's magnetotail (Delcourt et al., 2017; Ip, 1987; Sun et al., 2018). A previous study on the Earth's magnetotail also finds the dawn-dusk asymmetry in κ for both ions and electrons (Espinoza et al., 2018).

The results in Figure 4 ensure the occurrence of surface precipitation. Unlike the loss cone distribution in Earth's inner magnetosphere (Yue et al., 2017), the PADs in Mercury's magnetotail plasma sheet are not symmetric: The incident flux is almost isotropic from 0° to 90° while the reflected flux decreases from 90° to 180° (Figure 1h). A possible cause of the isotropic incident flux is the pitch angle scattering of protons in the central plasma sheet which is consistent with the nonzero flux within the loss cone (170° to 180°, Figure 1h). The loss flux is predominantly contributed by the thermal component of protons, which agrees with the pitch angle scattering explanation since the thermal protons have larger gyro-radius and can be more efficiently scattered than the warm protons.

To summarize, we have statistically investigated the proton properties in Mercury's magnetotail plasma sheet by fitting the 5-year observations of FIPS data with the Gaussian-Kappa model. The main conclusions are listed as follows:

1. The proton spatial distributions reveal dawn-dusk asymmetry in proton's density, thermal pressure, and spectral index κ. The outward radial gradient in the proton temperature is also presented, which may suggest that the protons are energized when they are transported inward.
2. The open-closed field line boundary coincides with profiles of proton's number density, temperature, and integrated fluxes. Such distributions suggest that motion of protons in the outer plasma sheet are adiabatic. This is confirmed by the fact that the gyro-radii of protons are much smaller than the curvature radii of the magnetic field lines outside the central plasma sheet.
3. The occurrence of surface precipitation is confirmed by the asymmetric PAD of protons. The loss of protons is predominately contributed by thermal protons because of the stronger pitch angle scattering in the central plasma sheet. The loss ratios are revealed to be north-south asymmetric, which is likely attributed to the northward offset of Mercury's magnetic dipole center.

Data Availability Statement

MESSENGER data used in this study were available from the Planetary Data System (PDS): https://pds.jpl.nasa.gov; Magnetometer: https://pds-ppi.igpp.ucla.edu/search/view/?f=yes&id=pds://PPI/MESS-E_V_H_SW-MAG-3-CDR-CALIBRATED-V1.0; and Fast Imaging Plasma Spectrometer: https://pds-ppi.igpp.ucla.edu/search/view/?f=yes&id=pds://PPI/MESS-E_V_H_SW-EPPS-3-FIPS-DDR-V2.0.

References

Alexeev, I. I., Belenkaya, E. S., Slavin, J. A., Korth, H., Anderson, B. J., Baker, D. N., et al. (2010). Mercury's magnetospheric magnetic field after the first two MESSENGER flybys. *Icarus*, 209(1), 23–39. https://doi.org/10.1016/j.icarus.2010.01.024
Anderson, B. J., Acuña, M. H., Korth, H., Slavin, J. A., Uno, H., Johnson, C. L., et al. (2010). The magnetic field of Mercury. *Space Science Reviews*, 152(1), 307–339. https://doi.org/10.1007/s11214-009-9544-3

Anderson, B. J., Acuña, M. H., Lohr, D. A., Scheifele, J., Raval, A., Korth, H., & Slavin, J. A. (2007). The magnetometer instrument on MESSENGER. *Space Science Reviews*, *131*(1), 417–450. https://doi.org/10.1007/s11214-007-9246-7

Anderson, B. J., Johnson, C. L., Korth, H., Purucker, M. E., Winslow, R. M., Slavin, J. A., et al. (2011). The global magnetic field of Mercury from MESSENGER orbital observations. *Science*, *333*(6051), 1859–1862. https://doi.org/10.1126/science.1211001

Anderson, B. J., Johnson, C. L., Korth, H., Winslow, R. M., Borovsky, J. E., Purucker, M. E., et al. (2012). Low-degree structure in Mercury's planetary magnetic field. *Journal of Geophysical Research*, *117*, E00L12. https://doi.org/10.1029/2012JE004159

Andrews, G. B., Zurbuchen, T. H., Mauk, B. H., Malcom, H., Fisk, L. A., Gloeckler, G., et al. (2007). The energetic particle and plasma spectrometer instrument on the MESSENGER spacecraft. *Space Science Reviews*, *131*(1), 523–556. https://doi.org/10.1007/s11214-007-9272-5

Bchner, J., & Zelenyi, L. M. (1989). Regular and chaotic charged particle motion in magnetotaillike field reversals: 1. Basic theory of trapped motion. *Journal of Geophysical Research*, *94*(A9), 11,821–11,842. https://doi.org/10.1029/JA094iA09p11821

Chen, Y., Tth, G., Jia, X., Slavin, J. A., Sun, W., Markidis, S., & Raines, J. M. (2019). Studying dawn-dusk asymmetries of Mercury's magnetotail using MHD-EPIC simulations. *Journal of Geophysical Research: Space Physics*, *124*, 8954–8973. https://doi.org/10.1029/2019JA026840

Delcourt, D., Leblanc, F., Seki, K., Terada, N., Moore, T., & Fok, M. C. (2007). Ion energization during substorms at Mercury. *Planetary and Space Science*, *55*(11), 1502–1508. https://doi.org/10.1016/j.pss.2006.11.026

Delcourt, D. C., Malova, H. V., & Zelenyi, L. M. (2017). On the response of quasi-adiabatic particles to magnetotail reconfigurations. *Annales Geophysicae*, *35*(1), 11–23. https://doi.org/10.5194/angeo-35-11-2017

DiBraccio, G. A., Slavin, J. A., Imber, S. M., Gershman, D. J., Jackman, C. M., et al. (2015). MESSENGER observations of flux ropes in Mercury's magnetotail. *Planetary and Space Science*, *115*, 77–89. https://doi.org/10.1016/j.pss.2014.12.016

DiBraccio, G. A., Slavin, J. A., Raines, J. M., Gershman, D. J., Tracy, P. J., Boardsen, S. A., et al. (2015). First observations of Mercury's plasma mantle by MESSENGER. *Geophysical Research Letters*, *42*, 9666–9675. https://doi.org/10.1002/2015GL065805

Espinoza, C. M., Stepanova, M., Moya, P. S., Antonova, E. E., & Valdivia, J. A. (2018). Ion and electron distribution functions along the plasma sheet. *Geophysical Research Letters*, *45*, 6362–6370. https://doi.org/10.1029/2018GL078631

Gershman, D. J., Slavin, J. A., Raines, J. M., Zurbuchen, T. H., Anderson, B. J., Korth, H., et al. (2013). Magnetic flux pileup and plasma depletion in Mercury's subsolar magnetosheath. *Journal of Geophysical Research: Space Physics*, *118*, 7181–7199. https://doi.org/10.1002/2013JA019244

Gershman, D. J., Slavin, J. A., Raines, J. M., Zurbuchen, T. H., Anderson, B. J., Korth, H., et al. (2014). Ion kinetic properties in Mercury's pre-midnight plasma sheet. *Geophysical Research Letters*, *41*, 5740–5747. https://doi.org/10.1002/2014GL060468

Imber, S. M., & Slavin, J. A. (2017). MESSENGER observations of magnetotail loading and unloading: Implications for substorms at Mercury. *Journal of Geophysical Research: Space Physics*, *122*, 11,402–11,412. https://doi.org/10.1002/2017JA024332

Ip, W. H. (1987). Dynamics of electrons and heavy ions in Mercury's magnetosphere. *Icarus*, *71*(3), 441–447. https://doi.org/10.1016/0019-1035(87)90039-X

Jasinski, J. M., Slavin, J. A., Raines, J. M., & DiBraccio, G. A. (2017). Mercury's solar wind interaction as characterized by magnetospheric plasma mantle observations with MESSENGER. *Journal of Geophysical Research: Space Physics*, *122*, 12,153–12,169. https://doi.org/10.1002/2017JA024594

Korth, H., Anderson, B. J., Gershman, D. J., Raines, J. M., Slavin, J. A., Zurbuchen, T. H., & McNutt Jr., R. L. (2014). Plasma distribution in Mercury's magnetosphere derived from MESSENGER magnetometer and fast imaging plasma spectrometer observations. *Journal of Geophysical Research: Space Physics*, *119*, 2917–2932. https://doi.org/10.1002/2013JA019567

Korth, H., Tsyganenko, N. A., Johnson, C. L., Philpott, L. C., Anderson, B. J., Al Asad, M. M., & McNutt Jr., R. L. (2015). Modular model for Mercury's magnetospheric magnetic field confined within the average observed magnetopause. *Journal of Geophysical Research: Space Physics*, *120*, 4503–4518. https://doi.org/10.1002/2015JA021022

Poh, G., Slavin, J. A., Jia, X., Raines, J. M., Imber, S. M., Sun, W.-J., et al. (2017a). Coupling between Mercury and its nightside magnetosphere: Cross-tail current sheet asymmetry and substorm current wedge formation. *Journal of Geophysical Research: Space Physics*, *122*, 8419–8433. https://doi.org/10.1002/2017JA024266

Poh, G., Slavin, J. A., Jia, X., Raines, J. M., Imber, S. M., Sun, W.-J., et al. (2017b). Mercury's cross-tail current sheet: Structure, X-line location and stress balance. *Geophysical Research Letters*, *44*, 678–686. https://doi.org/10.1002/2016GL071612

Poh, G., Slavin, J. A., Jia, X., Sun, W.-J., Raines, J. M., Imber, S. M., et al. (2018). Transport of mass and energy in Mercury's plasma sheet. *Geophysical Research Letters*, *45*, 12,163–12,170. https://doi.org/10.1029/2018GL080601

Potter, A., & Morgan, T. (1985). Discovery of sodium in the atmosphere of Mercury. *Science*, *229*(4714), 651–653. https://doi.org/10.1126/science.229.4714.651

Raines, J. M., Gershman, D. J., Zurbuchen, T. H., Sarantos, M., Slavin, J. A., Gilbert, J. A., et al. (2013). Distribution and compositional variations of plasma ions in Mercury's space environment: The first three Mercury years of MESSENGER observations. *Journal of Geophysical Research: Space Physics*, *118*, 1604–1619. https://doi.org/10.1029/2012JA018073

Raines, J. M., Slavin, J. A., Zurbuchen, T. H., Gloeckler, G., Anderson, B. J., Baker, D. N., et al. (2011). MESSENGER observations of the plasma environment near Mercury. *Planetary and Space Science*, *59*(15), 2004–2015. https://doi.org/10.1016/j.pss.2011.02.004

Rong, Z. J., Ding, Y., Slavin, J. A., Zhong, J., Poh, G., Sun, W. J., et al. (2018). The magnetic field structure of Mercury's magnetotail. *Journal of Geophysical Research: Space Physics*, *123*, 548–566. https://doi.org/10.1002/2017JA024923

Russell, C. T., & Walker, R. J. (1985). Flux transfer events at Mercury. *Journal of Geophysical Research*, *90*(A11), 11,067–11,074. https://doi.org/10.1029/JA090iA11p11067

Scurry, L., Russell, C. T., & Gosling, J. T. (1994). Geomagnetic activity and the beta dependence of the dayside reconnection rate. *Journal of Geophysical Research*, *99*(A8), 14,811–14,814. https://doi.org/10.1029/94JA00794

Siscoe, G. L., Ness, N. F., & Yeates, C. M. (1975). Substorms on Mercury? *Journal of Geophysical Research*, *80*(31), 4359–4363. https://doi.org/10.1029/JA080i031p04359

Slavin, J. A., Acuña, M. H., Anderson, B. J., Baker, D. N., Benna, M., Boardsen, S. A., et al. (2009). MESSENGER observations of magnetic reconnection in Mercury's magnetosphere. *Science*, *324*(5927), 606–610. https://doi.org/10.1126/science.1172011

Slavin, J. A., Anderson, B. J., Baker, D. N., Benna, M., Boardsen, S. A., Gloeckler, G., et al. (2010). MESSENGER observations of extreme loading and unloading of Mercury's magnetic tail. *Science*, *329*(5992), 665–668. https://doi.org/10.1126/science.1188067

Slavin, J. A., Anderson, B. J., Baker, D. N., Benna, M., Boardsen, S. A., Gold, R. E., et al. (2012). MESSENGER and Mariner 10 flyby observations of magnetotail structure and dynamics at Mercury. *Journal of Geophysical Research*, *117*, A01215. https://doi.org/10.1029/2011JA016900

Slavin, J. A., & Holzer, R. E. (1979). The effect of erosion on the solar wind stand-off distance at Mercury. *Journal of Geophysical Research*, *84*(A5), 2076–2082. https://doi.org/10.1029/JA084iA05p02076

Smith, A. W., Jackman, C. M., Frohmaier, C. M., Fear, R. C., Slavin, J. A., & Coxon, J. C. (2018). Evaluating single spacecraft observations of planetary magnetotails with simple Monte Carlo simulations: 2. Magnetic flux rope signature selection effects. *Journal of Geophysical Research: Space Physics*, *123*, 10,124–10,138. https://doi.org/10.1029/2018JA025959

Sun, W.-J., Fu, S. Y., Slavin, J. A., Raines, J. M., Zong, Q. G., Poh, G. K., & Zurbuchen, T. H. (2016). Spatial distribution of Mercury's flux ropes and reconnection fronts: MESSENGER observations. *Journal of Geophysical Research: Space Physics*, *121*, 7590–7607. https://doi.org/10.1002/2016JA022787

Sun, W.-J., Raines, J. M., Fu, S. Y., Slavin, J. A., Wei, Y., Poh, G. K., et al. (2017). MESSENGER observations of the energization and heating of protons in the near-Mercury magnetotail. *Geophysical Research Letters*, *44*, 8149–8158. https://doi.org/10.1002/2017GL074276

Sun, W.-J., Slavin, J. A., Dewey, R. M., Raines, J. M., Fu, S. Y., Wei, Y., et al. (2018). A comparative study of the proton properties of magnetospheric substorms at earth and Mercury in the near magnetotail. *Geophysical Research Letters*, *45*, 7933–7941. https://doi.org/10.1029/2018GL079181

Sun, W.-J., Slavin, J. A., Fu, S., Raines, J. M., Zong, Q.-G., Imber, S. M., et al. (2015). MESSENGER observations of magnetospheric substorm activity in Mercury's near magnetotail. *Geophysical Research Letters*, *42*, 3692–3699. https://doi.org/10.1002/2015GL064052

Sundberg, T., Slavin, J. A., Boardsen, S. A., Anderson, B. J., Korth, H., Ho, G. C., et al. (2012). MESSENGER observations of dipolarization events in Mercury's magnetotail. *Journal of Geophysical Research*, *117*, A00M03. https://doi.org/10.1029/2012JA017756

Winslow, R. M., Anderson, B. J., Johnson, C. L., Slavin, J. A., Korth, H., Purucker, M. E., et al. (2013). Mercury's magnetopause and bow shock from MESSENGER magnetometer observations. *Journal of Geophysical Research: Space Physics*, *118*, 2213–2227. https://doi.org/10.1002/jgra.50237

Wurz, P., Gamborino, D., Vorburger, A., & Raines, J. M. (2019). Heavy ion composition of Mercury's magnetosphere. *Journal of Geophysical Research: Space Physics*, *124*, 2603–2612. https://doi.org/10.1029/2018JA026319

Yue, C., Bortnik, J., Thorne, R. M., Ma, Q., An, X., Chappell, C. R., & Kletzing, C. A. (2017). The characteristic pitch angle distributions of 1 eV to 600 keV protons near the equator based on Van Allen Probes observations. *Journal of Geophysical Research: Space Physics*, *122*, 9464–9473. https://doi.org/10.1002/2017JA024421

Zhao, J. T., Sun, W. J., Zong, Q. G., Slavin, J. A., Zhou, X. Z., Dewey, R. M., et al. (2019). A statistical study of the force balance and structure in the flux ropes in Mercury's magnetotail. *Journal of Geophysical Research: Space Physics*, *124*, 5143–5157. https://doi.org/10.1029/2018JA026329

Zurbuchen, T. H., Raines, J. M., Slavin, J. A., Gershman, D. J., Gilbert, J. A., Gloeckler, G., & Solomon, S. C. (2011). MESSENGER observations of the spatial distribution of planetary ions near Mercury. *Science*, *333*(6051), 1862–1865. https://doi.org/10.1126/science.1211302